Alumina Particle Reinforced Cu Matrix Conductors

Ke Han, Robert E. Goddard, Vince Toplosky, Rongmei Niu, Jun Lu, and Robert Walsh

***Abstract*—The high strength conductors used in pulsed magnets in the US National High Magnetic Field Laboratory (MagLab) are manufactured from Cu matrix composites. One of the composites is made from particle-reinforced Cu. The fabrication of these composite conductors requires high deformation strain, which creates high densities of dislocations and reduced particle spacing. Both mechanical strength and electrical conductivity can be predicted from particle spacing and dislocation density. When dislocation density reaches a certain value, the particle size, distribution, and shape become important to mechanical properties. We studied the particle size, distribution, and shape in high-strength conductors with respect to the properties of the conductors. The two most important factors related to the above parameters were dislocations near the interface between particle and matrix and stress concentration near the particles. By engineering these variations, the properties of the conductors can be optimized. This paper reports our understanding of the relationship between critical properties and particle distribution in composite conductors for high field pulsed magnets.**

***Index Terms*—High strength conductor, pulsed magnet, coil winding, failure mode, plastic deformation.**

I. Introduction

GLIDCOP is the trademark for a line of dispersion-strengthened copper conductors favored for use in resistive DC magnets, pulsed magnets, and fusion applications [1]–[3]. GlidCop conductors are made from Cu-Al alloy powders that have been internally oxidized to produce alumina (Al_2O_3) particles [4].

Researchers have used three methods to consolidate the powder into bulk conductors: hot isostatic pressing (HIP), extrusion (Ex), and extrusion followed by deformation (Ex+Def). All those methods are followed by annealing. The deformation can be either by drawing or by rolling. This Ex+Def approach produces materials with the highest ductility and fracture toughness [5]. Therefore, most GlidCop conductors are made by the Ex+Def method.

GlidCop is stronger than pure Cu [6]. It also has higher creep resistance [7]. At temperatures below 500 °C, GlidCop retains its high strength even at temperatures below 500 [8]. Researchers have found that heat treatment has little impact on microstructure [9], [10]. They have reported that heat treating the rolled alloy at high temperature decreases the mechanical strength and increases the ductility of GlidCop conductors even when microstructure is not greatly affected. This is similar to Cu-Ag and Cu-Nb composite conductors [11].

Deformation strengthens GlidCop [12]. Because GlidCop has higher strength than pure Cu, it is more susceptible to cracking in stress concentrated regions [13]. Therefore, cold deformation of GlidCop to a high degree of strain is more difficult for GlidCop than for Cu.

In fatigue tests, annealed GlidCop samples show both cyclic hardening and cyclic softening, but as-deformed samples show cyclic softening alone [10]. Because dislocation substructures are stabilized by alumina particles after deformation, softening is much slower in GlidCop than in pure Cu [13]. Thus, at high stress range, the fatigue life of GlidCop should be longer than that of Cu. At low amplitudes, the two are similar [13].

Deformed GlidCop shows anisotropy. In extruded samples, for example, mechanical strength and fatigue resistance are higher in the extrusion direction than in the transverse [12].

Researchers have reported that deformation results in the formation of cracks and in an increase in the number of pores, followed by de-cohesion of small alumina particles. The final fracture path is the result of a coalescence of previously originated cracks [14]. After equal channel angle press, initial cracks were seen to have formed in the middle of the specimen in triple junctions of grain boundaries, leading to de-cohesion of alumina particles followed by ultimate failure [14].

All the mechanical properties of GlidCop are governed by the size and distribution of the alumina particles. Srivatsan *et al.* reported that alumina particle sizes were between 3 and 12 nm with particle spacing between 30 and 100 nm [9]. Groza *et al.* reported an average size of 20 ± 5 nm with spacing of 34 ± 14 nm [15]. Ernest *et al.* reported that particles at the grain boundaries are α-alumina with size of 1 μm, and particles within the grains are cubic alumina with size of 100 nm [16]. This inconsistency in reported particle sizes calls for further studies. In our work, which was focused on alumina particle size and distribution in GlidCop, we found much larger particle size distribution than that reported by previous researchers in this area. We will discuss the reasons for this inconsistency.

II. Experimental Methods

A. Materials and Fabrication

GlidCop rods were received from North America Hoganas (NAH) in Ex+Def form. The Ex+Def rods were cold drawn at room temperature in either Sam Dong or our laboratory.

Manuscript received August 28, 2017; accepted December 21, 2017. Date of publication February 23, 2018; date of current version March 14, 2018. The work was supported in part by the National Science Foundation under Grant DMR-1157490, in part by the State of Florida, and in part by the U.S. Department of Energy. *(Corresponding author: Ke Han.)*

K. Han, R. E. Goddard, V. Toplosky, R. Niu, J. Lu, and R. Walsh are with the National High Magnetic Field Laboratory, Tallahassee, FL 32309 USA (e-mail: han@magnet.fsu.edu).

Color versions of one or more of the figures in this paper are available online at http://ieeexplore.ieee.org.

Digital Object Identifier 10.1109/TASC.2018.2795587

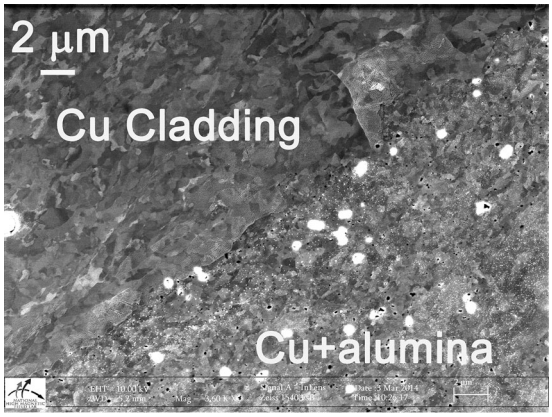

Fig. 1. SEM cross-section image taken by an in-lens detector showing microstructure of as-received GlidCop. Sample was cleaned by ion-beam to reveal the Cu grains. Cu cladding is at the upper left area and Cu+ alumina is at the lower right area. The image shows the size variation of the alumina particles.

The nominal content of alumina in GlidCop Al60 grade was 1.1 wt.% (1.62 vol.%)

B. Microstructure Examination

Microstructure was investigated in a Zeiss 1540EsB field emission gun scanning electron microscope (FEG SEM) at an accelerating voltage of 15 kV. For chemistry examinations, an Energy Dispersion X-ray (EDX) spectrometer was attached to the SEM. Transmission electron microscope (TEM) samples were prepared by jet-polishing. By means of a JEOL 002 ARM operating at 200 kV was used to carry out TEM observations.

C. Mechanical Properties

Mechanical tests were performed at 295 K and 77 K on a 100 kN servo-hydraulic MTS test machine. In tensile tests, the samples were loaded at a displacement control rate of 0.5 mm/min. An unload/reload cycle was performed to determine the elastic modulus. A 25 mm gage-length extensometer was used to record strain, and a 100 kN load cell to measure force.

III. Results

Both GlidCop Al15 and Al60 were investigated. Most results in this paper are related to Al60.

A. Alumina in As-Received Rods

Previous researchers used mainly TEM to identify alumina [9], [15], [16]. Current work shows that FEG SEM can also reveal alumina particles with sizes at nanometer scale. All surfaces of the GlidCop samples were cleaned by ion-beam. In order to enhance microstructure contrast.

As received GlidCop conductors contain both Cu cladding and Cu+ alumina core (Fig. 1). Under SEM, a boundary can be observed between these two components.

SEM images were compared with element-mapping images of aluminum and oxygen to identify the alumina in GlidCop (Fig. 2). Under optimized imaging conditions, the alumina in images taken by backscatter detector showed darker contrast than the matrix, while alumina in images taken by secondary detector or in-lens detector showed brighter contrast than the matrix (Fig. 2(a)). SEM results were later confirmed by TEM.

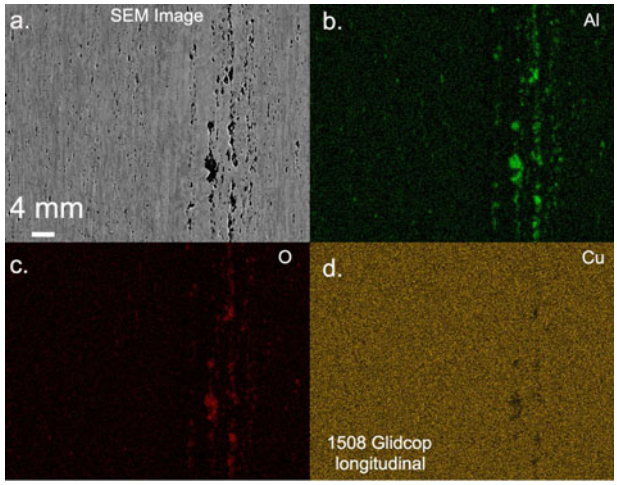

Fig. 2. SEM longitudinal cross-section image and EDX mapping of Cu + alumina. (a) SEM image taken by backscattered detector; (b) aluminum mapping; (c) oxygen mapping; (d) copper mapping. The dark clusters in (a) correspond to areas rich in both aluminum and oxygen, indicating the presence of alumina. In the imaged area, the minimum alumina size is about 5 nm and the maximum reaches 5 μm. The image also shows that the alumina is not distributed homogeneously. Larger particles are mainly found in the right-hand of each imaged area.

TABLE I
Mechanical Properties of AS-Received GlidCop AL15

Sample	Test T (K)	E (GPa)	YS (MPa)	TS (MPa)	Ef (%)	RA (%)
As-received	RT	90 ± 4	302 ± 9	378 ± 1	46 ± 1	80 ± 1
As-drawn	RT	101 ± 3	467 ± 20	497 ± 14	13 ± 2	42 ± 6
As-drawn	77	108 ± 6	569 ± 22	623 ± 18	20 ± 2	43 ± 4

T: temperature; E: elastic Young's modulus; YS: yield strength; TS: ultimate tensile strength; Ef: elongation at fracture; RA: reduction in area at fracture.

In longitudinal cross-section, SEM images showed alumina particles distributed along the wire direction, with sizes varying from 5 nm to 5 μm. The maximum alumina size we observed was larger than previously reported [9], [15], [16]. The size distribution of alumina particles is expected to affect both deformability and plastic deformation of GlidCop. Large-sized particles reduce the ductility of GlidCop. We mapped size distribution, volume fraction, and density of the alumina particles. Alumina particles appeared to be segregated by size, although the volume fraction remained almost the same (Fig. 3(a) and (b)). In areas with larger particles, density was low, possibly resulting in higher stress concentration, and therefore, lower ductility (see Fig. 3(d)). Conversely, areas with higher density of small particles are likely to have lower stress concentration, higher ductility, and therefore more capability for deformation (Fig. 3(c)).

The ductility of as-received rods was high and the variation of ductility was low within a batch (Table I). This indicates a low volume fraction in large particles, as observed by SEM.

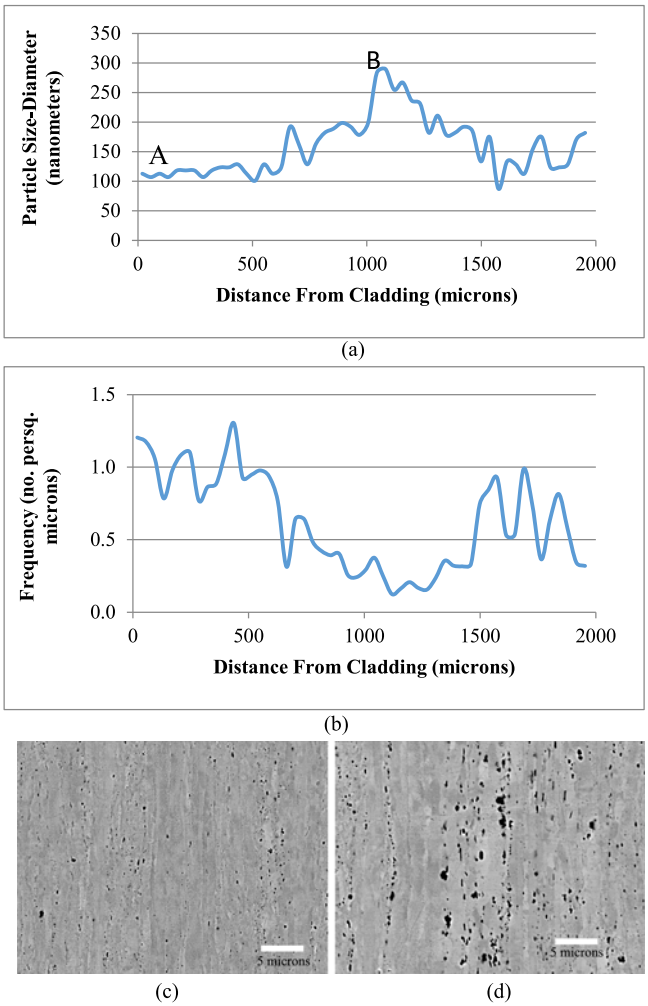

Fig. 3. Particle distribution in longitudinal cross-section of an as-received GlidCop Al60 (particles greater than 80 nm are shown in (a). The scale bar in (c) and (d) is the same). (a) Particle size distribution in an area between 20 μm and 2000 μm away from the Cu cladding area. (b) Particle frequency distribution in the same region as in (a). (c) Cross-section SEM backscattered image showing alumina particle distribution in location A in (a). (d) SEM backscattered image showing alumina particle distribution in location B in (a). Both images and data show that the size varies significantly, but the volume fraction remains similar in different regions.

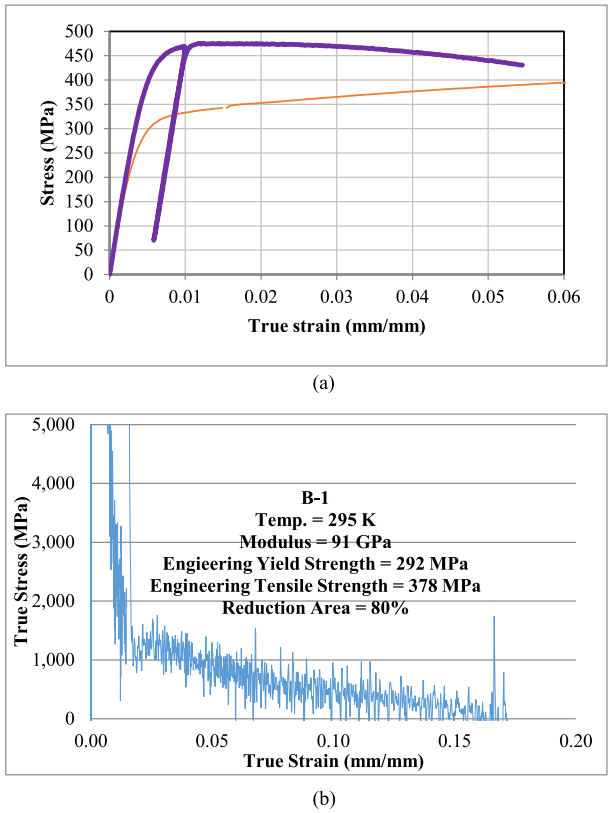

Fig. 4. (a) Typical true stress-strain curves of as-received (thin orange line) and as-drawn (thick pink line) samples. For as-drawn samples, the strain hardening rate, which is the slope of the stress-strain curves, becomes negative at strain of 2%. (b) A strain- hardening curve in as-received Al15. Strain-hardening rate remains positive at strain values greater than 15%.

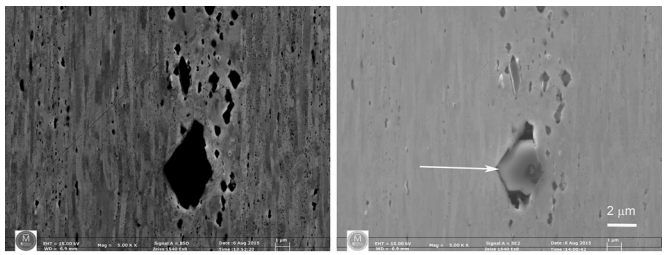

Fig. 5. Comparison of (a) a back-scattered electron image and (b) a second-electron image taken in SEM in the same area. The second electron image appears to show micro-voids formed between the alumina (indicated by an arrow) and the Cu matrix.

Young's modulus of GlidCop is lower than that of pure Cu. Stress-strain curves indicate that uniform elongation is higher than 15%, thus, this material can be deformed to 15% without instability (Fig. 4(a)).

At strain up to 5%, the strain hardening rate reaches above 1000 MPa (Fig. 4(b)). This value is significantly higher than for either coarse-grained or ultra-fine grained pure Cu (below 20 MPa) [17], [18]

B. Cold Drawn GlidCop

After cold deformation, the alumina particles in GlidCop Al60 are more oriented and elongated in the drawing direction than alumina particles observed in as-received samples. In all the samples we examined, coarser-sized particles tended to be concentrated in discrete zones of ~4 μm across the width of the cross section (Fig. 5). Close examination of the regions with large alumina particles revealed micro-voids above and below each of the particles in the drawing direction. This indicates the presence of high stress concentration in this region, which causes a disintegration of the interface between alumina particles and the Cu matrix. In our samples, we observed none of the de-cohesion of alumina particles during deformation that has been reported by previous researchers [14].

Because of its high strain hardening rate, the mechanical strength of cold drawn GlidCop is generally higher than that of either pure Cu or as-received GlidCop (Table I). Deformation also enhanced the Young's modulus by about 10%. We attributed this to texture formation during drawing.

TABLE II
PROPERTIES OF GLIDCOP AL60 AFTER DRAWING

	E (GPa)	YS (MPa)	TS (MPa)	Ef (%)	RA (%)	Cond (%IACS)
RT*	111	524	565	7	42	82
No. of tests	81	80	82	75	29	38
Stdev**	6	29	23	3	18	1
77 K data	120	655	733	13	34	357
No. of tests	145	144	146	115	46	38
Stdev	7	37	29	3	16	13

*RT: Test conducted at room temperatures.
**Stdev: Standard deviation of the tests.
Con: Conductivity in International Annealed Copper Standard.

TABLE III
PROPERTY COMPARISON OF GLIDCOP AL15 AND AL60

Sample	Test T (K)	YS (MPa)	TS (MPa)	Cond (%IACS)	RRR	TS/YS
Al60	RT	524 ± 29	565 ± 23	82 ± 1	4.3	1.08
Al60	77	655 ± 37	733 ± 29	357 ± 38	–	1.12
Al15	RT	467 ± 20	497 ± 14	92*	–	1.06
Al15	77	569 ± 22	623 ± 18	–	–	1.10

RRR: Ratio of room temperature resistance over that at 77 K.
*Value reported by Höganäs AB.

After deformation, ductility was reduced. Elongation and reduction-in-area at fracture were reduced by 71% and 48%, respectively. The reduced ductility is partially attributable to the voids formed during deformation (Fig. 5). The remaining ductility, however, was sufficiently high for winding most of the magnets in US National High Magnetic Field Laboratory.

C. Deformation Behaviors at Cryogenic Temperatures

At 77 K, GlidCop Al15 samples show 7% higher Young's modulus, 22% higher yield strength, and 26% higher tensile strength than at room temperature (Table I). Elongation also has a higher value at cryogenic temperatures, although reduction-in-area at fracture remains the same. This indicates that overall ductility remains the same, but the strain hardening rate is higher at cryogenic temperatures.

Because of inhomogeneity of particle distribution in GlidCop Al60, a large number of mechanical tests must be conducted before these conductors can be used in pulsed magnets (Table II). At both room temperature and 77 K, cold-drawn GlidCop Al60 conductors showed higher elastic Young's modulus and mechanical strength than Al15 (Table III). These two materials both show large elongation at fracture.

IV. DISCUSSION

A. Alumna Particle Size

Our work indicates that the size of alumina particles can reach several micrometers in local areas. This is significantly larger than reported in previous work. Larger particles are sparsely distributed in the matrix and can thus be easily overlooked without a large area scan. Most previous researchers have used TEM, which is more appropriate for scanning smaller areas. For this reason, large particles may have not been adequately reported in previous work.

Large particles observed in GlidCop appear to have no significant impact on ductility in materials deformed to relatively small strain. During large strain deformation, however, de-cohesion may occur between alumina and the Cu matrix, resulting in failure of the GlidCop.

B. Property Assessment

Most studies of GlidCop have been focused on room temperature properties. This current work includes mechanical properties at both room and cryogenic temperatures. Because pulsed magnets operate at 77 K and conductor temperature can reach a value close to room temperature in the same magnet. GlidCop shows high values for Young's modulus, yield strength, tensile strength, and ductility at 77 K. That is why most GlidCop conductors performe well when commissioned in high field pulsed magnets operating at 77 K.

Both Al15 and Al60 have been used in high-field pulsed magnets. Both materials show higher strength than pure Cu, close to the level achievable in bulk Cu strengthened by nano-twins [19]–[23]. Both conductors show higher TS/YS ratios at 77 K, indicating higher strain hardening rates. The ratio, however, is lower than either Cu-Ag or Cu-Nb [17], [18], [20]–[22], [24]–[41]. Al15 has higher electrical conductivity but lower mechanical strength.

V. SUMMARY

Alumina particles in GlidCop conductors were examined by FEG SEM. In images taken by backscattered electron detectors, small alumina particles showed darker contrast than the matrix. In images taken by secondary electron or in-lens detector, however, these particles sometimes showed brighter contrast. Particles ranging in size from 5 nm to 5 μm were distributed along the wire direction. The larger particles, which accounted for a small volume fraction, were sparsely distributed in the matrix. Increasing alumina volume fraction and cold-deformation-strain would enhance Young's modulus and mechanical strength. At 77 K, GlidCop conductors showed higher values than at room temperature with respect to Young's modulus, yield strength, tensile strength, and elongation. The reduction-in-area at fracture, however, remained the same. This indicates that overall ductility remains the same, but strain hardening rates are higher at 77 K, thus enhancing mechanical strength and homogeneous elongation.

ACKNOWLEDGMENT

We thank Dr. Tyler for editing the manuscript, Drs. Nguyen and Mielke for discussions, Höganäs AB for supplying composites, and Sam Dong for wire drawing.

REFERENCES

[1] T. Asano *et al.*, "Resistive insert magnet for a 37.3-T hybrid magnet," *Physica B*, vol. 294, pp. 635–638, Jan. 2001.

[2] R. R. Solomon *et al.*, GlidCop AL-25 first wall plates-IG1 grade compared to IG0 grade, in *Proc. 17th IEEE/NPSS Symp. Fusion Eng.*, 1998, pp. 853–857.

[3] L. Li *et al.*, "Design of a large-bore 60-T pulse magnet for Sandia National Laboratories," *IEEE Trans. Appl. Supercond.*, vol. 10, no. 1, pp. 530–533, Mar. 2000.

[4] J. D. Troxell, A. V. Nadkarni, and R. R. Solomon, "Properties and performance of GlidCop (R) DSC in temperature range of 20–350°C," in *Process. Fabrication Advanced Mater. V*, 1996, pp. 755–774.

[5] R. R. Solomon, J. D. Troxell, and A. V. Nadkarni, "GlidCop DSC properties in the temperature range of 20–350 °C," *J. Nuclear Mater.*, vol. 233, pp. 542–546, Oct. 1996.

[6] T. J. Miller, S. J. Zinkle, and B. A. Chin, "Strength and fatigue of dispersion-strengthened copper," *J. Nuclear Mater.*, vol. 179, pp. 263–266, Mar./Apr. 1991.

[7] S. E. Broyles *et al.*, "Creep deformation of dispersion-strengthened copper," *Metallurgical Mater. Trans. A—Phys. Metallurgy Mater. Sci.*, vol. 27, no. 5, pp. 1217–1227, May 1996.

[8] H. C. deGroh, D. L. Ellis, and W. S. Loewenthal, "Comparison of GRCop-84 to other Cu alloys with high thermal conductivities," *J. Mater. Eng. Perform.*, vol. 17, no. 4, pp. 594–606, Aug. 2008.

[9] T. S. Srivatsan, S. Anand, and J. D. Troxell, "Influence of High-treatment on microstructure and tensile properties of GlidCop dispersion strengthened copper alloy," *Mater. Lett.*, vol. 14, no. 1, pp. 11–16, Jun. 1992.

[10] T. S. Srivatsan, M. Al-Hajri, and J. D. Troxell, "The tensile deformation, cyclic fatigue and final fracture behavior of dispersion strengthened copper," *Mech. Mater.*, vol. 36, no. 1/2, pp. 99–116, Jan./Feb. 2004.

[11] B. Z. Cui, Y. Xin, and K. Han, "Structure and transport properties of nanolaminate Cu-Nb composite foils by a simple fabrication route," *Scripta Mater.*, vol. 56, no. 10, pp. 879–882, May 2007.

[12] A. Daoud *et al.*, "Anisotropy effects on the tensile and fatigue behaviour of an oxide dispersion strengthened copper alloy," *Mater. Sci. Eng. A—Struct. Mater. Prop. Microstruct. Process.*, vol. 534, pp. 640–648, Feb. 2012.

[13] J. Robles *et al.*, "Low-cycle fatigue of dispersion-strengthened copper," *Metallurgical Mater. Trans. A—Phys. Metallurgy Mater. Sci.*, vol. 25, no. 10, pp. 2235–2245, Oct. 1994.

[14] M. Besterci *et al.*, "Fracture mechanisms of GlidCop Cu-Al_2O_3 composite before and after ECAP observed by "in-situ tensile test in SEM"," *Kovove Materialy—Metallic Mater.*, vol. 51, no. 6, pp. 383–387, 2013.

[15] J. Groza and S. Farrens, "Microstructural studies of internally oxidized copper alloys," *Microstruct. Sci.*, pp. 689–699, 1991.

[16] F. Ernst, P. Pirouz, and A. H. Heuer, "HRTEM study of a Cu/Al_2O_3 interface," *Philosoph. Mag. A—Phys. Condensed Matter Struct. Defects Mech. Prop.*, vol. 63, no. 2, pp. 259–277, Feb. 1991.

[17] Y. H. Zhao *et al.*, "Simultaneously increasing the ductility and strength of ultra-fine-grained pure copper," *Adv. Mater.*, vol. 18, no. 22, p. 2949-+, Nov. 2006.

[18] K. Han, "Property of ultrafine grained engineering materials related to high magnetic fields," in *Proc. TMS Annu. Meet.*, 2006, 473–480.

[19] B. Z. Cui *et al.*, "Highly textured and twinned Cu films fabricated by pulsed electrodeposition," *Acta Mater.*, vol. 55, no. 13, pp. 4429–4438, Aug. 2007.

[20] R. M. Niu and K. Han, "Strain hardening and softening in nanotwinned Cu," *Scripta Mater.*, vol. 68, no. 12, pp. 960–963, Jun. 2013.

[21] R. M. Niu *et al.*, "Influence of grain boundary characteristics on thermal stability in nanotwinned copper," *Scientific Rep.*, vol. 6, Aug. 2016.

[22] R. M. Niu *et al.*, "Atomic-scale studies on the effect of boundary coherency on stability in twinned Cu," *Appl. Phys. Lett.*, vol. 104, no. 1, Jan. 2014.

[23] L. Brandao *et al.*, "Development of high strength pure copper wires by cryogenic deformation for magnet applications," *IEEE Trans. Appl. Supercond.*, vol. 10, no. 1, pp. 1284–1287, Mar. 2000.

[24] K. Han *et al.*, "Properties of high strength Cu-Nb conductor for pulsed magnet applications," *IEEE Trans. Appl. Supercond.*, vol. 12, no. 1, pp. 1176–1180, Mar. 2002.

[25] Y. Leprince-Wang *et al.*, "Microstructure in Cu-Nb microcomposites," *Mater. Sci. Eng. A—Struct. Mater. Prop. Microstruct. Process.*, vol. 351, no. 1/2, pp. 214–223, Jun. 2003.

[26] K. Han *et al.*, "Cold-deformed Cu-Ag and Cu-Nb composites," in *Proc. Ultrafine Grained Mater. Symp. III*, 2004, pp. 273–278.

[27] K. Han *et al.*, "Fatigue property examinations of conductors for pulsed magnets," *IEEE Trans. Appl. Supercond.*, vol. 20, no. 3, pp. 1463–1466, Jun. 2010.

[28] K. Han *et al.*, "High strength conductors for high field magnets," in *Proc. TMS 141st Annu. Meet. Exhib. – Supplemental Proc.* (Materials Properties, Characterization, and Modeling, vol. 2), 2012, pp. 521–528.

[29] J. Chen *et al.*, "Deformation behavior of Nb_3Sn type superconductors," *IEEE Trans. Appl. Supercond.*, vol. 15, no. 2, pp. 3568–3571, Jun. 2005.

[30] S. Downey, P. N. Kalu, and K. Han, "The effect of heat treatment on the microstructure stability of modified 316LN stainless steel," *Mater. Sci. Eng. A—Struct. Mater. Prop. Microstruct. Process.*, vol. 480, no. 1-2, pp. 96–100, May 2008.

[31] G. M. Li *et al.*, "Influence of high magnetic field on as-cast structure of Cu-25wt%Ag alloys," *China Foundry*, vol. 10, no. 3, pp. 162–166, May 2013.

[32] L. Qu *et al.*, "Studies of electrical resistivity of an annealed Cu-Fe composite," *J. Appl. Phys.*, vol. 113, no. 17, May 2013.

[33] X. W. Zuo *et al.*, "Microstructure and properties of nanostructured Cu-28wt% Ag microcomposite deformed after solidifying under a high magnetic field," *Mater. Sci. Eng. A—Struct. Mater. Prop. Microstruct. Process.*, vol. 619, pp. 319–327, Dec. 2014.

[34] X. W. Zuo. *et al.*, "Precipitation and dissolution of Ag in ageing hypoeutectic alloys," *J. Alloys Compounds*, vol. 622, pp. 69–72, Feb. 2015.

[35] X. W. Zuo *et al.*, "Microstructural dependence of magnetoresistance in CuAg alloy solidified with high magnetic field," *J. Mater. Process. Technol.*, vol. 224, pp. 208–212, Oct. 2015.

[36] K. Han *et al.*, "High strength conductors and structural materials for high field magnets," *MRS Adv.*, vol. 1, no. 17, pp. 1233–1239, 2016.

[37] C. C. Zhao *et al.*, "Simultaneously increasing strength and electrical conductivity in nanostructured Cu-Ag composite," *Mater. Sci. Eng. A—Struct. Mater. Prop. Microstruct. Process.*, vol. 652, pp. 296–304, Jan. 2016.

[38] X. W. Zuo *et al.*, "Microstructure and properties of Cu-6wt% Ag composite thermomechanical-processed after directionally solidifying with magnetic field," *J. Alloys Compounds*, vol. 676, pp. 46–53, Aug. 2016.

[39] X. W. Zuo *et al.*, "Nucleation and growth of gamma-Fe precipitate in Cu-2% Fe alloy aged under high magnetic field," *J. Alloys Compounds*, vol. 662, pp. 355–360, Mar. 2016.

[40] C. C. Zhao *et al.*, "Strength of Cu-28 wt%Ag composite solidified under high magnetic field followed by cold drawing," *Metals Mater. Int.*, vol. 23, no. 2, pp. 369–377, Mar. 2017.

[41] X. W. Zuo *et al.*, "Influence of Fe addition on microstructure and properties of Cu-Ag composite," *Metals Mater. Int.*, vol. 23, no. 5, pp. 974–983, Sep. 2017.